On the impact of the antenna radiation patterns in passive radio sensing

Federica Fieramosca, Vittorio Rampa, *Senior Member, IEEE*, Stefano Savazzi, *Member, IEEE*, and Michele D'Amico, *Senior Member, IEEE*

***Abstract*—Electromagnetic (EM) body models based on the scalar diffraction theory allow to predict the impact of subject motions on the radio propagation channel without requiring a time-consuming full-wave approach. On the other hand, they are less effective in complex environments characterized by significant multipath effects. Recently, emerging radio sensing applications have proposed the adoption of smart antennas with non-isotropic radiation characteristics to improve coverage. This letter investigates the impact of antenna radiation patterns in passive radio sensing applications. Adaptations of diffraction-based EM models are proposed to account for antenna non-uniform angular filtering. Next, we quantify experimentally the impact of diffraction and multipath disturbance components on radio sensing accuracy in environments with smart antennas.**

***Index Terms*—EM body model, scalar diffraction, antenna radiation pattern, passive radio sensing, device-free radio sensing**

I. Introduction

PASSIVE or device-free radio sensing is an opportunistic technique that employs stray ambient signals from Radio Frequency (RF) devices to detect, locate, and track people that do not carry any electronic device [1], [2]. The effect of the presence of body obstacles on the received RF signals is a well-know topic in the wireless communications community [3]–[5]. However, only recently, radio sensing techniques have been proposed to provide sensing capabilities, while performing radio communication according to the *Communication while Sensing* paradigm [2].

Quantitative evaluation [6]–[9], [11], [12] of perturbations due to the presence or movements of people (*i.e.,* the targets) has paved the way to the exploitation of electromagnetic (EM) models for passive radio sensing. In fact, the body-induced perturbations that impair the radio channel, can be acquired, measured, and processed using model-based methods to estimate location [13], and tracking target info [9], [10], or to assess location accuracy during network pre-deployment [14].

However, a general EM model for the prediction of body-induced effects on propagation is still under scrutiny [15], or too complex to be of practical use for real-time sensing scenarios [7], [16]. Simpler human-body shadowing models have been recently proposed for Device-Free Localization (DFL) based on scalar diffraction theory [11], [12].

This work is partially supported by the EU. Grant Agreement No: 101099491

F. Fieramosca and M. D'Amico are with Politecnico di Milano, DEIB department, e-mail: {federica.fieramosca,michele.damico}@polimi.it.

V. Rampa and S. Savazzi are with Consiglio Nazionale delle Ricerche (CNR), IEIIT institute, e-mail: {vittorio.rampa,stefano.savazzi}@ieiit.cnr.it.

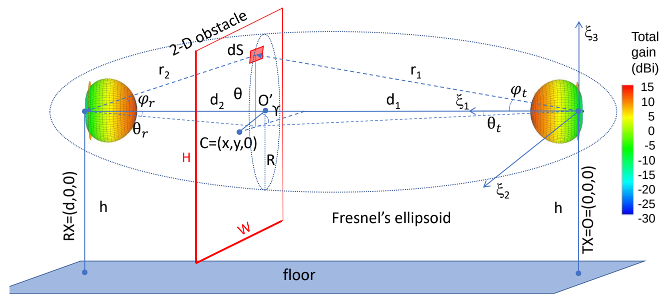

Figure 1: EM model geometry: 2-D obstacle and antennas.

Other semi-empirical models [17]–[19] have been also proposed for DFL applications [20]–[23]. However, these models require lengthy calibration pre-processing steps and will not be considered here (see [2], [13] for references).

II. Paper contributions

Considering the interest in novel Wireless Local Area Network (WLAN) sensing systems [24]–[27] and tools [28], with devices leveraging antennas with non-uniform [29]–[31], and/or re-configurable [32] radiation characteristics, it is deemed necessary to develop effective EM models [10], [19] that meet these emerging needs. Most of the previous tools were based on diffraction methods [9], [12], [16] and targeted devices equipped with omnidirectional antennas, with the exception of [33] that focused on human blockage at 73 GHz with the body represented as a semi-infinite rectangular shape and the paraxial approximation [11] being used.

The key ideas discussed in this letter are: *i*) the proposal of a simple human-body shadowing model, that includes also the antenna directivity characteristics; *ii*) the application of the proposed model in passive radio sensing and validation of its predictive potential; and *iii*) the evaluation of the impact of antenna radiation patterns by exploiting real on-field measurements in an indoor reflective environment. The paper is organized as follows: Sect. III presents a EM body model that includes the directional radiation pattern hypothesis while Sect. IV analyzes the body-induced effects in scenarios with mixed antenna systems (*i.e.,* both directional and omnidirectional). Sect. V validates the proposed body model in real field scenarios. Finally, Sect. VI draws some conclusions and proposes additional investigations.

III. EM body models

In this work, the statistical body model proposed in [11] for isotropic antennas is extended to take into account directional antennas with an assigned radiation pattern. We consider a single body, but the extension to multi-body scenarios can be inferred according to [12], [34]. We also assume that the body is in the Fraunhofer's regions of the antennas of the transmitter (TX) and receiver (RX): the regions start ≈ 25 cm away from the directional and ≈ 15 cm from the omnidirectional antennas of the experimental setup shown in Sect. IV.

As shown in Fig. 1, the 3-D shape of the human body is modeled as a 2-D rectangular absorbing sheet S [11] of height H and traversal size W, and has nominal position coordinates (x, y), w.r.t. the TX position, namely the projection of its barycenter on the horizontal plane. The scalar diffraction theory [35], [36] quantifies the impact of this obstruction. First, a distribution of Huygens' sources of elementary area dS is assumed to be located on the absorbing sheet. Then, the electric field $E = E_0 - \int_S dE$ at the RX is obtained by subtracting the contribution of the Huygens' sources $\int_S dE$ from the electric field E_0 of the free-space scenario (*i.e.,* with no target in the link area).

Using the received electric field E_0 under free-space condition as reference, for both isotropic antennas, we get [11]:

$$\frac{E}{E_0} = 1 - j\,\frac{d}{\lambda}\int_S \frac{1}{r_1\, r_2}\,\exp\left\{-j\frac{2\pi}{\lambda}\left(r_1 + r_2 - d\right)\right\} d\xi_2\, d\xi_3, \tag{1}$$

where d is the link length, $\lambda = c/f$ is the wavelength, while f is the frequency and c is the speed of light. Notice that each elementary source $dS = d\xi_2\, d\xi_3$ has distance r_1 and r_2 from the TX and RX, respectively.

The received power P is defined at the generic frequency f, omitted here for clarity, as:

$$P = \begin{cases} P_0 + w_0 & \text{free-space only} \\ P_0 - A_{\mathrm{S}}(x,y) + w_T & \text{with target } S, \end{cases} \tag{2}$$

where $A_{\mathrm{S}}(x,y) = -10\,\log_{10}|E\,/\,E_0|^2$ is the extra-attenuation due to the presence of S at coordinates (x, y). The free-space power P_0 is a constant that depends only on the link geometry and on the propagation coefficients: it is assumed to be known, or measured. The log-normal multipath fading and the other disturbances are modeled as the Gaussian noise terms $w_0 \sim \mathcal{N}\big(0, \sigma_0^2\big)$, with variance σ_0^2, and $w_T \sim \mathcal{N}\big(\mu_T, \sigma_T^2\big)$, with mean $\mu_T = \Delta h_T$ and variance $\sigma_T^2 = \sigma_0^2 + \Delta\sigma_T^2$, respectively. Δh_T and $\Delta\sigma_T^2 \geq 0$ are the residual stochastic fading terms that depend on the specific scenario as in [11].

For a generic non-isotropic antenna, equation (1) must be modified to take into account the antenna radiation pattern $G(\theta, \varphi) = G_0\, f(\theta, \varphi)$, where G_0 is the gain and $f(\theta, \varphi)$ is the normalized radiation pattern, while θ and φ are the polar coordinates, usually referred to the antenna phase center. First, we consider an isotropic RX antenna and a directional TX one that is pointed in the Line Of Sight (LOS) direction, with normalized radiation pattern $f_t(\theta_t, \varphi_t)$ and polar coordinates $\theta_t = \theta_t(r_1, r_2)$ and $\varphi_t = \varphi_t(r_1, r_2)$ w.r.t. the TX antenna phase center. The field ratio E/E_0 in (1) becomes:

$$\begin{aligned} \frac{E}{E_0} = 1 - j\,\frac{d}{\lambda}\int_S \frac{1}{r_1\, r_2}\,\sqrt{f_t(\theta_t, \varphi_t)}\,\cdot \\ \cdot\,\exp\left\{-j\frac{2\pi}{\lambda}\left(r_1 + r_2 - d\right)\right\} d\xi_2\, d\xi_3. \end{aligned} \tag{3}$$

Table I: SA settings and directional antenna specs.

Spectrum analyzer settings		Antenna specs	
Start/Stop Frequency	2.4/2.5 GHz	**HPBW** (θ)	H: 60°
Frequency spacing	1.25 MHz	**HPBW** (φ)	V: 76°
Resolution BW	100 kHz	**Polarization**	Vertical
TX output power	0 dBm	**Antenna gain**	9 dBi

If the receiving antenna is also directional and pointed toward the transmitter in the LOS direction, the received signal can be calculated, with good approximation, by weighting the contributions from the elementary Huygens' sources with the square root of the receiving antenna radiation pattern. If V and V_0 are the complex voltages at the RX antenna connector in the actual scenario and in free-space, respectively, we get:

$$\begin{aligned} \frac{V}{V_0} = 1 - j\,\frac{d}{\lambda}\int_S \frac{1}{r_1\, r_2}\,\sqrt{f_t(\theta_t, \varphi_t)\; f_r(\theta_r, \varphi_r)}\,\cdot \\ \cdot\,\exp\left\{-j\frac{2\pi}{\lambda}\left(r_1 + r_2 - d\right)\right\} d\xi_2\, d\xi_3, \end{aligned} \tag{4}$$

where $\theta_r = \theta_r(r_1, r_2)$ and $\varphi_r = \varphi_r(r_1, r_2)$ are the polar coordinates w.r.t. the receiving antenna phase center. Eq. (4) is derived from (3) by noting that V and V_0 are linearly dependent on E and E_0, respectively, through the effective antenna length. In this link configuration, the extra-attenuation for target in (x, y) is now given by $A_{\mathrm{S}}(x,y) = -10\,\log_{10}|V\,/\,V_0|^2$.

IV. Body-induced effects with mixed antennas

The measurement sessions took place in a hall with size 6.15 m $\times$ 14.45 m and floor-ceiling height equal to 3.35 m. As shown in Fig. 2, TX and RX nodes are spaced $d = 4.00$ m apart, while the LOS is horizontally placed at $h = 0.99$ m from the floor. Most surfaces are highly reflective, which cause poor DFL performances with omnidirectional antennas [11]. The goal is to verify the predictive capacity of the model in such complex conditions. The received power P is measured using a real-time Spectrum Analyzer (SA) [37] with a built-in tracking generator. The SA tracks $N_f = 401$ frequency points equally spaced with $\Delta f = 1.25$ MHz and settings as in Tab. I.

In what follows, three scenarios are analyzed featuring: *i)* the *omni-omni*, where both TX and RX antennas are omnidirectional; *ii)* the *omni-dir*, where only the TX is equipped with a directional antenna; and *iii)* the *dir-dir*, where both antennas are directional. Directional antennas operate at frequency band $2.4-2.5$ GHz: other specs [38] are summarized in Tab. I. Omnidirectional antennas are vertical monopoles with 2 dBi gain. To compare the measurements against the model predictions, we modeled the body as an absorbing rectangular 2-D sheet with height $H = 2.0$ m and traversal size $W = 0.55$ m (see Fig. 1). The maximum transversal size (*i.e.,* minor axis) of the first Fresnel's ellipsoid is about 0.70 m, while the beam width (at -3 dB) of each directional antenna is about 2 m at the same point (d_1=d_2=$d/2$).

The free-space received power $P_0(f_k)$ is obtained for each frequency of the set $\{f_k\}_{k=1}^{N_f}$. The received power $P(f_k, \ell)$ is then measured with the target located in each of the $\ell = 1, ..., 75$ marked positions of the grid points of Fig. 2. Each position ℓ has coordinates (x_ℓ, y_ℓ) with spacing 0.25 m along and 0.3 m across the LOS. The measured attenuation, due

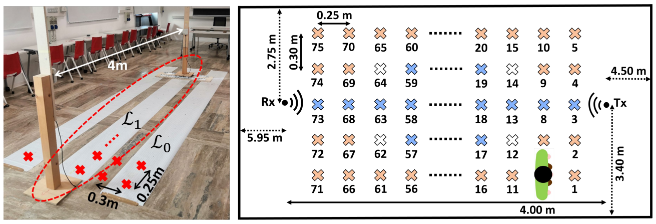

Figure 2: 75 marked positions (crosses) on a 15×5 grid with spacing 0.25 m along and 0.30 m across the link. Target is located at position 6 (drawing not to scale). Corresponding measurement scenario is on the left.

to the target in the ℓ-th position, is evaluated for each f_k as $A_{\mathrm{S},k}^{(m)}(\ell) = -10 \log_{10} [P(f_k, \ell) \,/\, P_0(f_k)]$ and then averaged to obtain the mean attenuation $A_{\mathrm{S}}^{(m)}(\ell) = 1/N_f \sum_{k=1}^{N_f} A_{\mathrm{S},k}^{(m)}(\ell)$.

The color-coded maps in Figs. 3.a, 3.b, and 3.c show the attenuation values for each subject position. For the *omni-omni* case of Fig. 3.a, the maximum value of attenuation is ≈ 4 dB. The body effect is thus negligible, except for positions very close to the antennas, due to a substantial amount of energy that reaches the RX antenna via multipath even if the first Fresnel's ellipsoid is blocked. On the contrary, in the *dir-dir* scenario of Fig. 3.c, the maximum attenuation reaches ≈ 16 dB, and the body presence near the LOS is clearly discernible. In fact, by using well-pointed directional antennas, the multipath impact is strongly reduced thanks to the angular filtering properties of the radiation patterns $f(\theta, \varphi)$. This scenario is thus closer to the ideal free-space environment with no disturbances. The *omni-dir* scenario of Fig. 3.b shows an intermediate behavior for some noticeable effects caused by multipath disturbances not filtered by the RX antenna. The maximum attenuation reaches ≈ 10 dB near the TX.

Measurements and predictions for the *omni* (1) and *dir* (4) setups are compared in Fig. 3 (bottom). The predictions are obtained by averaging $A_{\mathrm{S}}^{(p)}(\ell) = 1/N_p \sum_{k=1}^{N_p} A_{\mathrm{S}}(x_\ell + \triangle x_k, y_\ell + \triangle y_k)$ over the attenuations $A_{\mathrm{S}}(\cdot, \cdot)$ corresponding to N_p small body movements around the marked positions ℓ. The goal is to let the models account for body position uncertainties as well as small, involuntary movements typically observed in human sensing [11], [12]. We set $\triangle x_k, \triangle y_k \sim \mathcal{U}_{-\frac{\triangle}{2}, \frac{\triangle}{2}}$ as uniformly distributed in the interval $\triangle = 6$ cm, and $N_p = 150$. The measured $A_{\mathrm{S}}^{(m)}(\ell)$ (dashed lines) and the predicted $A_{\mathrm{S}}^{(p)}(\ell)$ (solid lines) average attenuations are compared w.r.t. 5 marked positions along two orthogonal cuts taken 0.25 m (orange lines) and 1 m (violet lines) from the TX antenna, respectively, with marks $\ell = 1 \div 5$ and $\ell = 16 \div 20$ (Fig. 2). The vertical bars include 60% of the measured values that cover the antenna operating band of $2.4 - 2.5$ GHz ($N_f = 81$). Accordingly, EM predictions are obtained for f_k in the same $2.4 - 2.5$ GHz band but use the field ratio (1) for omnidirectional antennas (square markers) and (4) for directional ones (cross markers). Shaded areas include 60% of the attenuation samples used to obtain the average terms $A_{\mathrm{S}}^{(p)}(\ell)$. Overall, the measurements reveal large fluctuations of the attenuations when the target is near the LOS path, while the *dir-dir* setup is close (on average) to the directional antenna predictions. In general, there is a negligible

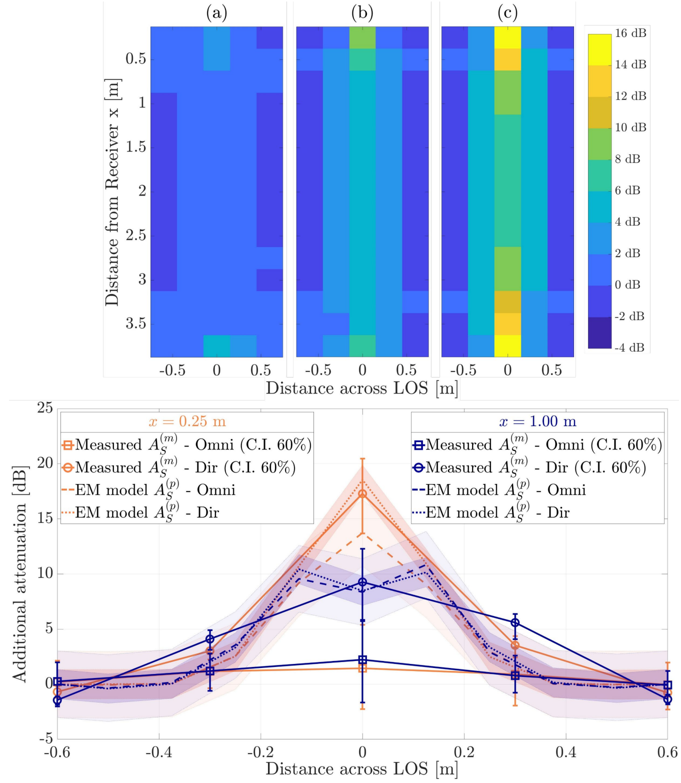

Figure 3: Top: maps of the measured attenuation (in dB) for each of the 75 points of the a) *omni-omni*, b) *omni-dir*, and c) *dir-dir* scenarios. Bottom: measured $A_{\mathrm{S}}^{(m)}$ (dashed) vs. predicted $A_{\mathrm{S}}^{(p)}$ (solid) average attenuations for a target traversing orthogonal to the LOS at 0.25 m (orange) and 1 m (violet) away from the TX. Model (1) with square markers and (4) with cross markers.

difference between *omni* and *dir* models when the target is far from the TX ($x_\ell > 1$ m) since the extra-attenuation is mainly due to the blockage of the first Fresnel's ellipsoid. Instead, a more marked difference is observed when the target moves close to the TX ($x_\ell = 0.25$ m) since the antenna beamwidth is now comparable with the Fresnel's area. The *omni* model over-estimates the attenuation obtained from the *omni-omni* setup due to the presence of multipath, as explained before.

V. Body detection and model validation

We discuss here the problem of passive body localization in the environment previously analyzed. The detection problem focuses on the choice between the hypotheses F_0 and F_1 that correspond to the target outside or inside the Fresnel's ellipsoid of the link, respectively. According to Fig. 2, we split the 75 inspected positions in two groups: namely, the $|\mathcal{L}_1| = L_1 = 25$ positions ($\ell \in \mathcal{L}_1$, blue crosses) that fall inside the Fresnel's ellipsoid, and the $|\mathcal{L}_0| = L_0 = 38$ positions ($\ell \in \mathcal{L}_0$, red crosses) that fall outside. At time t, the decision whether the target is inside or outside the Fresnel's ellipsoid is based on the extra-attenuation $A_{\mathrm{S}} = P_0 - P(t)$ that is observed w.r.t. the free-space power P_0 (in dBm). Omitting time t for clarity,

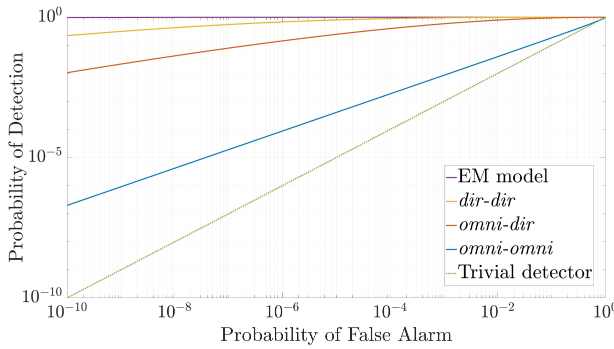

Figure 4: ROC plots considering the probabilities related to the EM model, and to the measurements from the *omni-omni*, *omni-dir* and *dir-dir* cases. The trivial detector is shown, too.

Table II: Likelihood separation and KL divergence.

	EM models ($A_{\mathrm{S}}^{(p)}$) (***omni-omni*/*dir-dir***)	**Measurements** ($A_{\mathrm{S}}^{(m)}$) (***omni-omni*/*omni-dir*/*dir-dir***)
$\mu_{\mathrm{F}_0} - \mu_{\mathrm{F}_1}$	9.2 dB/9.6 dB	1.8 dB/6.7 dB/11.9 dB
$\mathrm{KL}(\mathrm{F}_0 \| \mathrm{F}_1)$	2.59/2.60	1e−4/0.69/2.44

the Log-Likelihood Ratio (LLR):

$$\Gamma(A_{\mathrm{S}}) = \log\left[\frac{\Pr\left(A_{\mathrm{S}}\,|\mathrm{F}_1\right)}{\Pr\left(A_{\mathrm{S}}\,|\mathrm{F}_0\right)}\right] \tag{5}$$

is used to discriminate (via thresholding on Γ) between both hypotheses. Probabilities $\Pr\left(A_{\mathrm{S}}\,|\mathrm{F}_0\right) \sim \mathcal{N}(\mu_{\mathrm{F}_0}, \sigma^2_{\mathrm{F}_0})$ and $\Pr\left(A_{\mathrm{S}}\,|\mathrm{F}_1\right) \sim \mathcal{N}(\mu_{\mathrm{F}_1}, \sigma^2_{\mathrm{F}_1})$ are log-normal distributed. The parameters μ_{F_0} and μ_{F_1} model the average attenuations terms, while $\sigma_{\mathrm{F}_0} = \sigma_0$ and $\sigma_{\mathrm{F}_1} = \sigma_0 + \Delta\sigma_T$ are the deviations. Assuming no prior information about the subject location, it is also $\Pr\left(\mathrm{F}_0\right) = \Pr\left(\mathrm{F}_1\right) = 1/2$. Using the log-normal model (2), (5) can be rewritten as:

$$\Gamma(A_{\mathrm{S}}) = \frac{1}{2}\left(\frac{A_{\mathrm{S}} - \mu_{\mathrm{F}_0}}{\sigma_{\mathrm{F}_0}}\right)^2 - \frac{1}{2}\left(\frac{A_{\mathrm{S}} - \mu_{\mathrm{F}_1}}{\sigma_{\mathrm{F}_1}}\right)^2 - \log\left(\frac{\sigma_{\mathrm{F}_1}}{\sigma_{\mathrm{F}_0}}\right). \tag{6}$$

The LLR parameters are obtained from the predictions $A_{\mathrm{S}}^{(p)}(\ell)$ of Sect. III, namely $\mu_{\mathrm{F}_i} \approx \mu_{\mathrm{F}_i}^{(p)} = 1/L_i \sum_{\ell \in \mathcal{L}_1} A_{\mathrm{S}}^{(p)}(\ell)$ and $\sigma_{\mathrm{F}_i} \approx \sigma_{\mathrm{F}_i}^{(p)} = \sqrt{1/L_i \sum_{\ell \in \mathcal{L}_i} \left[A_{\mathrm{S}}^{(p)}(\ell) - \mu_{\mathrm{F}_i}^{(p)}\right]^2}$, for hypotheses F_0 and F_1. The fading effects [11], *i.e.* $\Delta h_T = 0$ are also neglected to highlight the diffraction terms only. For comparison, the LLR parameters are also obtained from measurements, $\mu_{\mathrm{F}_i} \approx \mu_{\mathrm{F}_i}^{(m)}$ and $\sigma_{\mathrm{F}_i} \approx \sigma_{\mathrm{F}_i}^{(m)}$, by replacing $A_{\mathrm{S}}^{(p)}(\ell)$ with $A_{\mathrm{S}}^{(m)}(\ell)$.

In Fig. 4, we analyze the Receiver Operating Characteristic (ROC) figures [39], using the LLR as in (6), for all scenarios. The ROC associated to the *dir-dir* scenario is the one with the best performance, being closer to the EM model predictions. The trivial detector implements a random choice. Considering that ROC performances depend on the LLR decision regions, *i.e.* the separation of the log-likelihood (LL) functions [39], in Fig. 5, we compare the LLs $\Pr\left(A_{\mathrm{S}}\,|\mathrm{F}_1\right)$ and $\Pr\left(A_{\mathrm{S}}\,|\mathrm{F}_0\right)$ for *omni-omni* (top) and *dir-dir* scenarios (bottom) obtained from experimental data ($\mu_{\mathrm{F}_i}^{(m)}$,$\sigma_{\mathrm{F}_i}^{(m)}$) and predictions ($\mu_{\mathrm{F}_i}^{(p)}$, $\sigma_{\mathrm{F}_i}^{(p)}$) using synthetic data, respectively. In Tab. II we also report

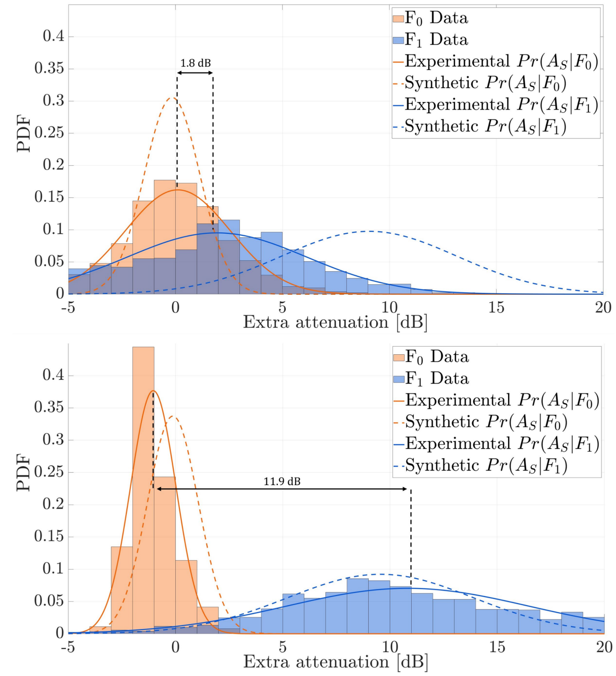

Figure 5: From top to bottom: estimated $\Pr(A_S|F_0)$ and $\Pr(A_S|F_1)$ from the experimental data and the synthetic (EM) model for the *omni-omni* (top) and the *dir-dir* scenarios (bottom). Histograms from experimental data are shown, too.

the average LL separation $\mu_{\mathrm{F}_0} - \mu_{\mathrm{F}_1}$ and the corresponding Kullback-Leibler (KL) divergence [40] using measured and predicted parameters. The decision regions for the *dir-dir* scenario are well separated (about $\mu_{\mathrm{F}_0}^{(m)} - \mu_{\mathrm{F}_1}^{(m)} = 11.9$ dB) and this is confirmed by the *dir* model (4) as $\mu_{\mathrm{F}_0}^{(p)} - \mu_{\mathrm{F}_1}^{(p)} = 9.6$ dB. Similarly, a KL divergence of 2.44 is predicted against the measured one of 2.6. The decision regions for the *omni-omni* setup are almost overlapped, with average separation of 1.8 dB and negligible KL divergence due to the multipath effects and the absence of any angular filtering. Such effects are not captured by the *omni* model which performs poorly.

VI. Conclusions

This letter proposes a human-body model that accounts for antennas with non-isotropic radiation characteristics and evaluates the impact of the radiation pattern for passive radio sensing. Diffraction and multipath components, that contribute to radio sensing accuracy, are evaluated experimentally in an indoor environment with mixed antenna configurations.

The angular filtering properties of directional antennas mitigate the multipath effects and make the propagation scenario closer to the results predicted by the diffraction-based EM model. Considering the problem of classifying target proximity, the model effectively predicts the separation of the decision regions, observed with directional antennas, for target inside or outside the Fresnel's ellipsoid. On the contrary, using omnidirectional antennas, the multipath effects dominate over diffraction and the model fails to predict such separation.

Future works will adapt the proposed model to Wireless LAN sensing devices leveraging antennas with software reconfigurable radiation characteristics.

References

[1] M. Youssef, et al., "Challenges: Device-free passive localization for wireless environments", Proc. 13th Annu. ACM Int. Conf. Mobile Comput. Netw. (MobiCom), pp. 222–229, 2007.

[2] S. Savazzi, et al., "On the use of stray wireless signals for sensing: A look beyond 5G for the next generation of industry", Computer, vol. 52, no. 7, pp. 25-36, July 2019.

[3] J. E. Brittain, "Albert Hoyt Taylor [Scanning the Past]", Proc. IEEE, vol. 82, no. 6, pp. 958, Jun. 1994.

[4] Z. Krupka, "The effect of the human body on radiation properties of small-sized communication systems", IEEE Transactions on Antennas and Propagation, vol. 16, no. 2, pp. 154-163, March 1968.

[5] H. King, et al., "Effects of a human body on a dipole antenna at 450 and 900 MHz", IEEE Transactions on Antennas and Propagation, vol. 25, no. 3, pp. 376–379, May 1977.

[6] M. Ghaddar, et al., "Human body modelling for prediction of effect of people on indoor propagation channel", Electronics Letters, vol. 40, no. 25, pp. 1592–31594, Dec. 2004.

[7] M. Ghaddar, et al., "A conducting cylinder for modeling human body presence in indoor propagation channel". IEEE Transactions on Antennas and Propagation, vol. 55, no. 11, pp. 3099–3103, Nov. 2007.

[8] G. Koutitas, "Multiple human effects in body area networks", IEEE Antennas and Wireless Propagation Letters, vol. 9, pp. 938–941, 2010.

[9] Z. Wang, et al., "A Diffraction Measurement Model and Particle Filter Tracking Method for RSS-Based DFL", IEEE Journal on Selected Areas in Communications, vol. 33, no. 11, pp. 2391–2403, Nov. 2015.

[10] O. Kaltiokallio, et al. "A Novel Bayesian Filter for RSS-Based Device-Free Localization and Tracking", IEEE Transactions on Mobile Computing, vol. 20, no. 3, pp. 780-795, March 2021.

[11] V. Rampa, et al., "EM models for passive body occupancy inference", IEEE Antennas and Wireless Propagation Letters, vol. 17, no. 16, pp. 2517–2520, 2017.

[12] V. Rampa, et al., "Electromagnetic Models for Passive Detection and Localization of Multiple Bodies", IEEE Transactions on Antennas and Propagation, vol. 70, no. 2, pp. 1462–1745, 2022.

[13] R.C. Shit, et al., "Ubiquitous Localization (UbiLoc): A Survey and Taxonomy on Device Free Localization for Smart World", IEEE Communications Surveys & Tutorials, vol. 21, no. 4, pp. 3532–3564, Fourthquarter 2019.

[14] S. Kianoush, et al., "Pre-deployment performance assessment of device-free radio localization systems", Proc. of the 2016 IEEE International Conference on Communications Workshops (ICC'16), pp. 1–6, 2016.

[15] B. R. Hamilton, et al., "Propagation modeling for radio frequency tomography in wireless networks", IEEE J. Sel. Topics Signal Process., vol. 8, no. 1, pp. 55–65, Feb. 2014.

[16] A. Eleryan, et al., "Synthetic generation of radio maps for device-free passive localization", Proc. of the IEEE Global Telecommunications Conference (GLOBECOM'11), pp. 1–5, 2011.

[17] S. Nannuru, et al., "Radio-frequency tomography for passive indoor multitarget tracking", IEEE Transactions on Mobile Computing, vol. 12, no. 12, pp. 2322–2333, 2012.

[18] Y. Guo, et al., "An exponential-Rayleigh model for RSS-based device-free localization and tracking", IEEE Transactions on Mobile Computing, vol. 14, no. 3, pp. 484–494, 2014.

[19] A. Abdelgawwad, et al. "A Trajectory-Driven 3D Channel Model for Human Activity Recognition", IEEE Access, vol. 9, pp. 103393-103406, 2021

[20] J. Wilson, et al., "Radio tomographic imaging with wireless networks", IEEE Trans. on Mobile Comp., vol. 9, no.5, pp. 621–632, May 2010.

[21] M. Mohamed, et al., "Physical-statistical channel model for off-body area network", IEEE Antennas and Wireless Propagation Letters, vol. 16, pp. 1516–1519, 2017.

[22] J. Wang, et al., "Device-free localisation with wireless networks based on compressive sensing", IET Communications, vol. 6, no. 5, pp. 2395–2403, Oct. 2012.

[23] A.S.A. Sukor, et al., "RSSI-Based for Device-Free Localization Using Deep Learning Technique", Smart Cities, vol. 3, no. 2, pp. 444–455, 2020.

[24] V. Rampa, et al., "Electromagnetic Models for Device-Free Radio Localization with Antenna Arrays", Proc. of the IEEE-APS Topical Conference on Antennas and Propagation in Wireless Communications (APWC'22), pp. 1–5, Sept. 5–9, Cape Town, South Africa, 2022.

[25] D. Halperin, et al., "Predictable 802.11 packet delivery from wireless channel measurements", ACM SIGCOMM Computer Communication Review, vol. 41, no. 4, p. 159–170, 2011.

[26] Y. Xie, et al., "Precise power delay profiling with commodity Wi-Fi", IEEE Transactions on Mobile Computing, vol. 18, no. 6, pp. 1342–1355, 2018.

[27] S. Chauhan, et al., "IEEE 802.11be: A Review on Wi-Fi 7 Use Cases", Proc. of the 9th International Conference on Reliability, Infocom Technologies and Optimization (Trends and Future Directions) (ICRITO'21), pp. 1–7, 2021.

[28] M. Atif, et al., "Wi-ESP—A tool for CSI-based Device-Free Wi-Fi Sensing (DFWS)", Journal of Computational Design and Engineering, vol. 7, no. 5, pp. 644–656, Oct. 2020.

[29] L. Zhang, et al., "DeFi: Robust Training-Free Device-Free Wireless Localization With WiFi", IEEE Transactions on Vehicular Technology, vol. 67, no. 9, pp. 8822–8831, Sept. 2018.

[30] S. Shukri, et al., "Enhancing the radio link quality of device-free localization system using directional antennas", Proc. of the 7th International Conference on Communications and Broadband Networking, pp. 1–5, Apr. 2019.

[31] D. Garcia, et al., "POLAR: Passive object localization with IEEE 802.11 ad using phased antenna arrays", Proc. of the IEEE INFOCOM 2020-IEEE Conference on Computer Communications, pp. 1838–1847, Jul. 2020.

[32] M. Santoboni, et al., "Wireless LAN Sensing with Smart Antennas", Proc. of the 16th European Conference on Antennas and Propagation (EuCAP'22), pp. 1–5, Mar. 27–Apr. 01, Madrid, Spain, 2022.

[33] G. R. MacCartney, et al., "Millimeter-wave human blockage at 73 GHz with a simple double knife-edge diffraction model and extension for directional antennas", Proc. of the IEEE 84th Vehicular Technology Conference (VTC-Fall'16), pp. 1–6, Sept. 2016.

[34] V. Rampa et al., "Dual-target body model for device-free localization applications ", Proc. of the IEEE-APS Topical Conference on Antennas and Propagation in Wireless Communications (APWC'19), pp. 1–6, Sept. 2019.

[35] H. Mokhtari, et al., "Comparative study of lateral profile knife-edge diffraction and ray tracing technique using GTD in urban environment", IEEE Transactions on Vehicular Technology, vol. 48, no. 1, pp. 255–261, 1999.

[36] G. Durgin, "The practical behavior of various edge-diffraction formulas, "IEEE Antennas Propag. Mag., vol. 51, no. 3, pp. 24–35, Jun. 2009.

[37] RSA500 Series Real Time Spectrum Analyzers, [online], 2022, accessed: Sep. 27, 2022. Available: https://www.tek.com/en/products/spectrum-analyzers/rsa500.

[38] TP-LINK, User Guide, TL-ANT2409A 2.4 GHz 9 dBi Directional antenna, Rev. 1.0.2, 7106506238, [online], 2016, accessed: May 16, 2023. Available: https://static.tp-link.com/res/down/doc/TL-ANT2409A_V1_UG.pdf.

[39] T. Fawcett, "An introduction to ROC analysis,"Pattern Recognit. Lett., vol. 27, pp. 861–874, 2006.

[40] Kullback S, Leibler RA "On information and sufficiency," Ann Math Stat 22:79–86, 1951.